Majid Asli, Niclas Garan, Nicolai Neumann, Panagiotis Stathopoulos

A robust one-dimensional approach for the performance evaluation of turbines driven by pulsed detonation combustion

A robust one-dimensional approach for the performance evaluation of turbines driven by pulsed detonation combustion

Majid Asli[a,*], Niclas Garan[b], Nicolai Neumann[c], Panagiotis Stathopoulos[a]

[a] *TU Berlin, Institute of Fluid Dynamics and Technical Acoustics, Chair for Unsteady Thermodynamics in Gas Turbine Processes, Müller-Breslau-Straße 8, 10623 Berlin, Germany*
[b] *TU Berlin, Institute of Fluid Dynamics and Technical Acoustics, Chair of Combustion Kinetics, Müller-Breslau-Straße 8, 10623 Berlin, Germany*
[c] *TU Berlin, Institute of Aeronautics and Astronautics, Chair for Aero Engines, Marchstraße 12-14, 10587 Berlin, Germany*

Abstract

Among the solutions to reduce emissions from stationary gas turbines, replacing conventional combustion through pressure gain combustion is one of the most promising options. Nevertheless, coupling pressure gain combustion with a turbine can result in increased losses within the cycle, mainly because of the resulting very unsteady turbine inflow conditions. A reliable simulation tool can help to overcome this challenge and optimize turbine geometries and designs for the specific application. The harsh unsteady flow downstream of pressure gain combustors makes three-dimensional CFD computationally expensive. Thus, the development of a fast computational method is crucial. This paper introduces and explores such an alternative methodology. A one-dimensional Euler gas dynamic approach is combined with blade source terms, computed out of a steady-state turbine meanline analysis. To evaluate the methodology, three-dimensional CFD simulations are performed in parallel and the results are compared with those of the 1-D method. The energy extraction of a turbine expander is computed with both methods for three different configurations of pulsed detonation combustor arrays connected at the turbine inlet. The results show that the proposed approach is capable of simulating the turbine in such an unsteady environment accurately. Additionally, it is indicated that around 45% of the total unsteadiness is damped throughout the first blade row, which is almost irrespective of the inlet fluctuation amplitude. Due to its accuracy and very low computational cost, the developed methodology can be integrated into optimization loops in the early design and development stages of turbomachinery for pressure gain combustion applications.

Keywords: Pressure gain combustion, unsteady simulation, turbine performance, 1D-Euler, pulsed detonation combustion

1. Introduction

The rapid increase in the average global temperature during the past decades has urged legislators to take actions to limit global warming. Curbing the adverse effect of climate change needs a profound decrease in green house gas emissions. The power and transportation sectors are responsible for a high share of the total global CO_2 emissions. According to the long-term air traffic forecasts by ICAO [1], the number of air passengers is expected to grow by 2.2 times by the next twenty years. Therefore, a radical enhancement in gas turbine engine efficiency is necessary, to provide flexible, dispatchable generation and the lowest

*Corresponding author
Email address: asli@campus.tu-berlin.de (Majid Asli)

possible emissions. Pressure gain combustion, either in the form of Rotating Detonation Combustion (RDC) or Pulsed Detonation Combustion (PDC), is one of the concepts that can cut the current gas turbine emissions significantly. In PGCs, the unsteady detonative combustion process can raise the total pressure by up to 30% compared to a 2-3 % total pressure loss caused by conventional combustion chambers [2, 3]. Average total pressure gain in the combustion process can improve the thermodynamic efficiency in a gas turbine cycle. Several researchers have focused on the integration of PGC into conventional gas turbines so far, whether in the form of RDC [4, 5], PDC [6, 7, 8] or overall thermodynamic cycle investigation [9]. Nevertheless, a remaining open question is the adaptation of turbine expanders to the unsteady PGC outlet flow with the aim to efficiently convert the exhaust gas energy into mechanical work. The gas turbine cycle efficiency is very sensitive to the component performances. Additionally, for a gas turbine with PGC, the cycle efficiency becomes even more sensitive to turbine efficiency because of the increased expansion ratio. Since turbine expanders are designed for steady inlet flows, they show relatively low performance when driven by the periodically unsteady harsh exhaust flow of PGCs [10]. Strong fluctuations in the thermodynamic quantities cause the turbine blades to work in far off-design conditions and exhibit low efficiencies.

To date, several authors have characterized the interaction of turbine blades with the flow of PGCs. Among experimental studies, Glaser et al. [10] investigated the performance of an array of multiple pulsed detonation combustors connected to an axial turbine. They showed that the efficiency of the PDC-driven turbine is decreased by increasing the combustion tube fill-fractions. Later, the experimental studies of Anand et al. [11] on the same setup but without bypass air focused on the effect of pulsing frequency, fill fraction, and rotor revolution frequency on the extracted power. Qiu et al. [12] performed experimental studies of a turbine connected to two PDC tubes directly that achieved 27% higher specific thrust than that of the traditional Brayton cycle systems. Within the scope of RDC and turbine interaction experimental investigation, Tellefsen [4] performed one of the first RDC-axial turbine tests. He placed convergent outlet sections on the RDC to study the effect of back pressure on its operation. Naples et al. [13] implemented an RDC into a T63 gas turbine and successfully ran the turbine for about 20 minutes. Their design incorporated an air dilution system to reduce the turbine inlet temperature and the pressure fluctuations. This way, they have proven the feasibility of operating an RDC with an existing turbine as a unit.

While the complex unsteady, high-temperature flow and compact geometry of PGCs present limitations in experimental measurement and visualization, numerical tools can provide deep insight into the PGC flow field. Van Zante et al. [14] performed a three-dimensional CFD simulation of a detonation tube–turbine interaction to evaluate average pressure transmission loss and turbine stage performance. They observed attenuation in pressure fluctuations through an aircraft engine axial turbine stage and reverse flow in the early stages of PDC blowdown. A full turbine stage unsteady CFD simulation was performed by Liu et al. [15] to characterize a supersonic turbine downstream of an RDC. They revealed that the main contributor to the unsteady loss mechanism was the leading edge shock waves. Asli et al. [16] studied the performance of a turbine stationary vanes downstream of an RDC using two-dimensional URANS simulation and showed a velocity angle fluctuation amplitude decay of more than 57%

by the vanes.

Although 3D-CFD tools have been proven very useful in PGC-turbine interaction studies, the highly unsteady nature of PGC exhaust flow requires high computational costs, specifically in multistage turbine configurations. Meanline methods in turbomachinery provide a fast tool for performance evaluation of turbomachines, but are limited to steady state analysis. Therefore, the need for a fast and reliable method for performance evaluation of turbomachinery integrated into a PGC has drawn the authors attention to the 1D-Euler approach. It has been shown to be appropriate for turbomachinery simulation in conventional applications [17, 18, 19]. Chiong et al. [20] integrated meanline and one-dimensional methods for prediction of pulsating performance of a turbocharger turbine, where unsteady flow makes 3D simulations time-consuming. Concerning PGC-compressor interaction, recently Dittmar and Stathopoulos [21] used the 1D-Euler method to simulate a multistage compressor connected to a zero-dimensional plenum representing a PDC array. They applied equally distributed blade source terms across the blade rows based on the overall compressor map, which is a very rough estimation of blade force specifically at off-design conditions. This study has been extended and further developed by Neumann et al. [22]. They used a mean line model to provide the source terms for the 1D unsteady Euler solver. At the same time, they coupled the compressor with an array of PDC tubes, which were in turn modelled with a reactive unsteady 1D-Euler code. This way, they managed to study the compressor operation with more realistic boundary conditions and also couple the compressor operation to the inlet boundary conditions of the PDC array. Within the scope of PGC-turbine interaction, the current research focuses on applying and evaluating an unsteady 1D approach to simulate a multistage turbine connected to a PDC by solving Euler equations with source terms. The current work is an extension and adaptation of the work presented from Neumann et al. [22]. To the knowledge of the authors, no such study has been carried out so far. The turbine blade row behavior and the propagation of flow unsteadiness across the turbine rows are studied and compared to the 3D-CFD simulation results. To allow for these simulations, a methodology to calculate PDC outlet conditions is introduced, which can then be used as boundary conditions for both the 3D-CFD and the Euler-based simulations. The objective is to show that the 1D-Euler approach with rather low complexity and computational cost can be used in the early design and optimization of turbine expanders working with PGCs, and here specifically with PDC arrays.

2. Models and Methods

The methodology of the current work includes integrating different simulation techniques for the PDC combustors, their connection to each other in an array constellation by using a plenum at their outlet and that for the turbine expander. All methods will be elaborated on in this section.

The pulsed detonation combustors are modelled with the same solver used for the turbine model. For both a solver for the unsteady 1D inviscid Euler equations with appropriate source terms is used. Mass and energy source terms are used in the combustors, while energy and force terms are used to model the blade forces in the turbine model. The meanline method for steady-state turbine performance estimation is utilized to compute source terms for the 1D-Euler equations that represent the blade rows. In parallel, three dimensional steady and unsteady CFD

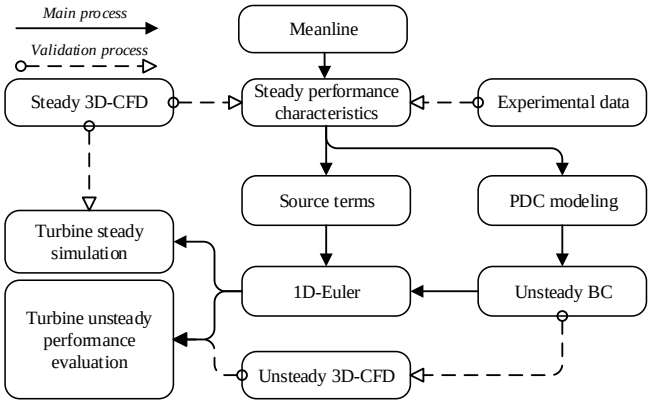

Figure 1: Overall flow chart of the simulations and the combination of the different tools

simulations are used to verify and tune the results of the mean line analysis and the 1D-Euler solver. It should be noted that, in the course of this paper, the CFD term is referred to as 3D-CFD.

The flow chart of Fig.1 shows how these methods are integrated. Firstly, using the geometrical specifications of the turbine, the map of the E^3 turbine geometry [23] is computed by both the meanline and 3D-CFD methods. Once the steady-state results are compared and validated against the experimental data, the source terms obtained by the meanline method are added to the 1D turbine model. Steady-state simulations are done using both 3D-CFD and 1D-Euler to check the agreement between the results in this step. Afterward, the PDC model uses the overall steady-state turbine map and provides the time-dependent inlet boundary conditions for unsteady turbine simulations. Finally, the 1D-Euler and 3D-CFD methods both simulate the turbine for the time-dependent operational case with the PDC arrays and the results are compared.

2.1. Test and reference case

The test case for the current work is the high-pressure turbine of the Energy Efficient Engine project reported by NASA [23]. This turbine is selected because it has two stages with available performance test results also between the blade rows, thus making it a vary useful validation and bench-marking test case. A summary of aerodynamic parameters of NASA E^3 high-pressure turbine at design point is listed in Table 1.

Table 1: Design point parameters of NASA E^3 high pressure turbine

Parameter	Value
Reduced mass flow ($kg\sqrt{K}$/s/kPa)	0.892
Reduced speed ($rpm/\sqrt{K}$)	316.9
Energy function ($J/kg/K$)	339.9
Pressure ratio	5.010
Efficiency	0.925

2.2. 3D-CFD method

The CFD analysis in this paper has been done by solving the unsteady three-dimensional Reynolds Averaged Navier–Stokes (RANS) equations using ANSYS CFX. The computational domain of the turbine is discretized using O and H grid types. The domain including the grids on surfaces is shown in Fig.2. Regarding the scope of the present study and the circumferentially uniform flow at the boundary conditions, a periodic-type interface is applied between the adjacent blade passages. The mixing plane approach is set as the interface between each blade row. This method assumes circumferentially averaged flow features in the outlet plane of the upstream row and uses them as the inlet condition of the downstream row. Since the PDC fluctuations are mainly in the axial direction, the stage mixing plan approach is valid for the present study as it has been applied in similar cases in [15, 21]. The mesh refinement close to the walls is done iteratively to keep y^+ below unity and to accurately capture boundary layer effects. To reduce the effect of grid size on the solution results, a mesh sensitivity study is done using four differ-

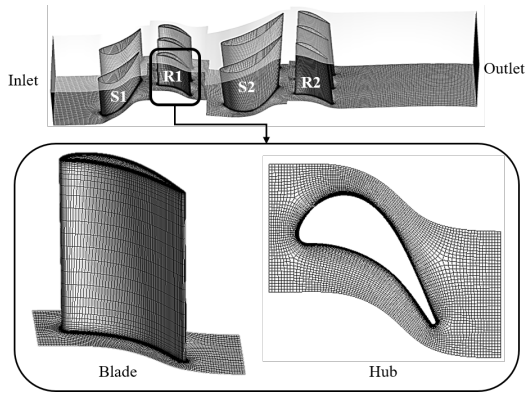

Figure 2: Turbine geometry model and a zoomed view of the computational grid

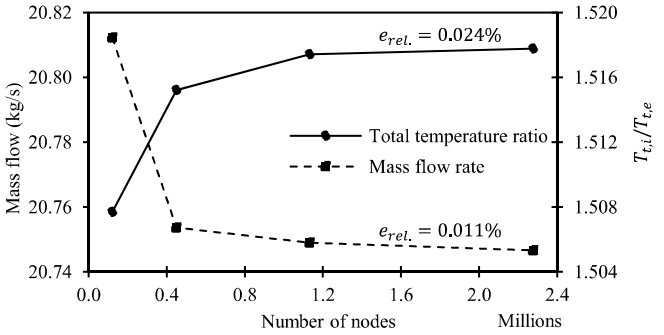

Figure 3: Effect of computational grid resolution on the computed mass flow rate and total temperature ratio

ent grid sizes having 122k, 449k, 1,132k, and 2,276k nodes, named as N_1 to N_4. Fig. 3 indicates mass flow rate and total temperature ratio for each grid size. The relative error representing the normalized difference between the two consecutive values ($e_{rel.} = (\phi_1 - \phi_2)/\phi_{mean}$) of results shown in the figure for the three finest grids. According to the results for N_3 and N_4, the relative error of mass flow and total temperature ratio are 0.011% and 0.024% respectively, which are very low. The Grid Convergence Index (GCI) is calculated following the approach presented by Celik et al. [24]. This parameter is an estimation to indicate how much further refinement of the computational grid can affect the results. The GCI values corresponding to N_3 are 0.1% and 0.2% for mass flow and total temperature ratio, respectively, which are low enough for an acceptable mesh size. Therefore, with regard to computational cost and accuracy, the computational domain with 1,132k nodes is selected for the current numerical study.

The Shear Stress Transport model, which is a two equations eddy viscosity approach, is used for turbulence modeling. The model combines the advantages of the k-ϵ and Wilcox k-ω model. The robustness of this turbulence modelling approach has been already proven for similar flows [25, 16]. For the time-dependent solution cases, the equations have been discretized in time with an implicit second-order Euler method. The second-order backward Euler method is applied to provide the transient scheme for turbulence equations.

Time step in transient solutions is a key parameter to capture the transient flow physics within the domain. A time step dependency analysis has been carried out for the current work using the transient inlet boundary condition caused by three PDC tubes. Considering the rotor blade passing frequencies ($\approx$ 15 kHz) and the PDC flow frequency ($\approx$ 100 Hz), three time step sizes were chosen, which are 500, 1000, and 2000 times smaller than the period of the inlet boundary condition fluctuations. The results of the simulations in terms of overall turbine efficiency are compared in Table 2. The relative change in efficiency decreases by lowering the time step size. The change between the two smaller time steps is deemed a negligible amount (0.02%) regarding the higher computational cost associated with the smallest time step. Therefore, a time step size of 10 µs is selected for all the transient simulations in the current study. Besides, periodic convergence must be fulfilled as part of a reliable unsteady simulation. Throughout this paper, the periodicity of the results at the domain outlet was monitored based on the method of Clark and Grover [26], which relies on the discrete Fourier

transform, cross correlation and Parseval's theorem. Once the overall convergence level (overall fuzzy set) for two consecutive cycles reaches a value greater or equal to 0.95, the transient solution is considered periodically converged.

Table 2: Effect of time step size on turbine efficiency

Time step (s)	2×10^{-5}	1×10^{-5}	5×10^{-6}
Efficiency	88.9	89.5	89.48
Relative change (%)	-	0.67	0.02
Pressure Ratio	5.110	5.132	5.133
Relative change (%)	-	0.43	0.03

2.3. Meanline method

Meanline method in turbomachinery is a well-known, simple, and reliable methodology for steady-state performance prediction, which remains popular today [27, 28, 29]. This method solves velocity triangles for every blade row on a reference radius of the machine and takes advantage of empirical correlations to account for energy loss in both design and off-design conditions. A schematic of velocity triangle and force vectors on a rotor blade is shown in Fig.4(a).

A meanline program has been coded for the current study, which includes the loss correlations from open literature most of which are reported and developed by Aungier [30]. The input matrix to the program contains the blades' geometrical parameters such as blade angle at leading and trailing edges, chord lengths, annulus radius, and rotational speed as well as total pressure and total temperature at the turbine inlet and static pressure at the outlet as the boundary conditions. The program starts with a pressure distribution guess through the machine and calculates the flow properties at each trailing edge in an entropy loop for each blade row. Once all the flow properties are computed, mass flow convergence is checked and the program continues by imposing a new pressure distribution using the target pressure method proposed by Denton [31] to reach a satisfactory convergence. Denton's method adjusts the pressure at each trailing edge based on the change in mass flow at one trailing edge downstream. Additionally, the Came's target pressure approach [32] is included where the Denton's method fails.

The results of the meanline program are used to compute the force and energy source terms representing every blade row in the 1D-Euler program for unsteady simulation. Therefore, it is very crucial that the code is able to accurately predict the flow features at inter-stages. The validity of the meanline program will be discussed in Sec.3.1.

2.4. 1D-Euler model

In general, the physics of the problem specify the required number of dimensions in its mathematical model. The nature of flow in turbomachinery shows that even one-dimensional modeling along the machine axis can provide a satisfactory model as the dominant flow phenomena occur in the axial direction. The time-dependent one-dimensional Euler solver utilized in the current work, for both the PDC model and the 1D turbine model, has been developed firstly for the purpose of shockless explosion combustion simulations [33]. It uses a finite volume scheme with a second-order monotonic upstream-centered scheme for conservation laws. The governing equations include the mass, momentum, and energy conversion equations, with source terms adjusted to meet the purpose of the corresponding component to be simulated.

2.4.1. 1D turbine model

To allow for the simulation of time-resolved turbomachinery applications, the original code was extended in the work of Dittmar and Stathopoulos [21] and in that of Neu-

mann et al. [22]. Within the course of the current research, this approach is further extended so that the calculation of the source terms representing the turbomachinery is now provided by the meanline method also for the turbine. The resulting governing equations are described in Eq.1, where Q is the matrix of source terms.

$$\frac{\partial B}{\partial t} + \frac{\partial G}{\partial x} = \frac{\partial Q}{\partial x} \tag{1}$$

$$B = \begin{bmatrix} \rho A \\ \rho V_x A \\ \rho E A \end{bmatrix}, G = \begin{bmatrix} \rho V_x A \\ \rho V_x^2 A + PA \\ \rho V_x A(\rho E + P) \end{bmatrix}, Q = \begin{bmatrix} \dot{m}_b \\ F_x + PA \\ W + \dot{m}_b h_{t,b} \end{bmatrix}$$

The source term to close the mass continuity equation is the bleed mass flow, which is assumed to be zero to simplify the simulations in this paper. Blade force and wall force represent the presence of blades and the force due to any change in cross-sectional area, respectively. Fig.4(b) shows the control volume and the force balance on it in a meridional view. According to the second law of motion, the net force acting on the control volume including the blade is equal to the momentum difference between the inflow and outflow. Therefore, the blade force can be computed as shown in Eq.2. The last three terms in Eq.2 are calculated based on the information from the meanline program. The endwall force is calculated within the 1D-Euler solver since it is included in the governing equations. The source terms in the energy equation are the shaft work by rotor blades and the enthalpy change due to the bleed (when applicable). The shaft work is calculated by the meanline data based on the first law of thermodynamics as described in Eq.3, noting that the blade row is assumed adiabatic and no heat is exchanged.

$$F_x = -F_{Endwalls} + F_{in} - F_{out} - \Delta(\dot{m}V_x) \tag{2}$$

where:

$$F_{in} = P_{in}A_{in} \quad \text{and} \quad F_{out} = P_{out}A_{out}$$

$$W = (\dot{m}h_t)_{out} - (\dot{m}h_t)_{in} \tag{3}$$

All source term related data for a range of steady-state operating points obtained by the meanline program is stored in a table. The 1D-Euler solver uses this table to extract the related force or work terms for each station in each iteration. Since the stored data is for discrete operating points of the turbine, the code has to interpolate the related source terms based on the calculated pressure at leading and trailing edge of the corresponding blade. To help the solution stability, the source term values are distributed based on an upside-down parabola function with the highest point at the blade axial center, which is shown in 4(b) graphically. The boundary conditions to the solver include total pressure and total temperature at the inlet and static pressure at the outlet. The computational domain is divided into 800 cells with a spatial resolution of Δx=0.5mm. The initial condition from which the transient simulation starts is provided by average values from the meanline result. The geometry is defined to the solver by specifying the axial coordinates of the inlet and the outlet of the domain, stator, and rotor blades as well as the annulus area at each axial location.

2.4.2. Pressure gain combustion model

To ensure that the boundary conditions for the 1D and 3D turbine simulations reflect conditions that can be ex-

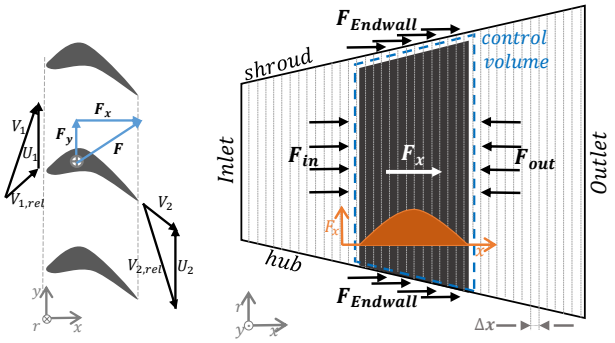

(a) Blade to blade view (b) Meridional view

Figure 4: View of a sample turbine rotor blade, (a): velocity triangle and blade force used in the meanline method (b): force source terms and control volume used in the 1D-Euler solver

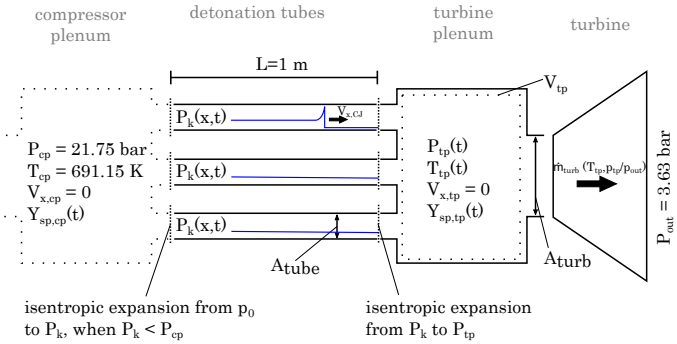

Figure 5: Multitube PDC model to obtain unsteady boundary condition

pected from PGC combustion as accurately as possible, a multitube PDC configuration was compiled. It combines several 1D PDC tubes with a zero-dimensional turbine plenum volume and a turbine model based on an interpolated turbine performance map. The complete numerical setup can be seen in Fig.5. The goal was to derive a time-dependent turbine plenum state that could be prescribed as a boundary condition in the two turbine models. Conceptually, this is an extension of the work done in [34], where in this case sinusoidal pressure fluctuations are replaced by a pressure evolution directly tied to each PDC tube. The approach is of course only a first approximation of the phenomena taking place within such a plenum that connects a PDC array and a turbine, but it can still capture the basic unsteadiness expected from such a setup.

Each detonation tube is represented by a one-dimensional domain that undergoes the typical PDC cycle schematically depicted in Fig.6. Every cycle starts with the ignition of the tube that is completely filled with a stoichiometric H_2–air mixture at the upstream end at ①. This ignition event is triggered by the insertion of a pre-computed detonation profile based on classic ZND theory [35, 36, 37] at the upstream end of the tube. The resulting detonation wave then proceeds to propagate downstream with CJ velocity in ②, consuming all remaining fuel and oxygen to form the combustion products (primarily N_2 and H_2O) at high temperature and pressure. With the outlet pressure far below the pressure of the combustion products, expansion waves reflect back and fourth through the domain as soon as the detonation wave has reached the outlet. Eventually, they reduce pressure far enough for it to fall below the upstream pressure and trigger the inlet to open in ③. First, an air buffer is introduced to separate hot products from fresh mixture. After purging of the combustion products, H_2 is added to the gas inflow in ④ to refill the tube and restart the cycle.

The number of tubes in the numerical setup can be varied. They all have a length of $L = 1\,\mathrm{m}$ and are ignited sequentially with an individual operating frequency of 20 Hz for each tube. The model assumes all PDC tubes to be fed by a common compressor plenum upstream, of which static pressure P_{cp} and static temperature T_{cp} are assumed constant and the flow velocity in it is assumed to be zero. T_{cp} and P_{cp} have been found to be the average values in the compressor plenum of a preliminary simulation that combined the compressor map provided in [38] with several detonation tubes. Air inflow from the compressor plenum to each of the PDC tubes is implemented as a one-way valve which remains closed for $P_k > P_{cp}$ and

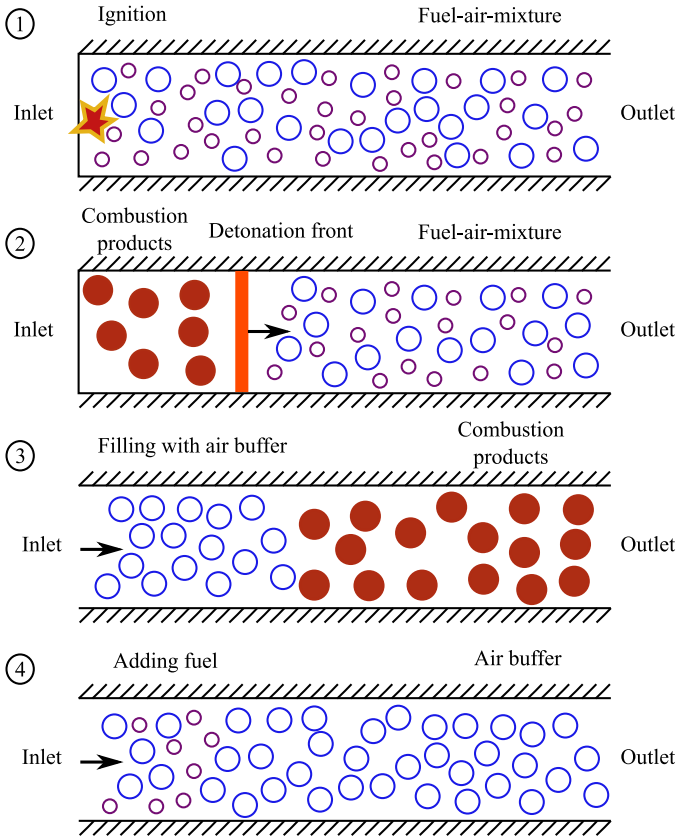

Figure 6: Single operating cycle of PDC tube

isentropically expands gas to downstream conditions in the k^{th} tube when $P_{cp} > P_k$. The chemical composition Y_{sp} of the inflowing gas is time-dependent for each tube and consists of pure air for the majority of each cycle and a stoichiometric H_2–air mixture during fill time ($t_{\text{fill}} = 10\,\text{ms}$).

Within each tube, the same 1D-Euler solver as for the 1D turbine model is used. However, balance equations and source term are modified and listed in Eq.4.

$$\frac{\partial B^*}{\partial t} + \frac{\partial G^*}{\partial x} = Q^* \tag{4}$$

$$B^* = \begin{bmatrix} \rho \\ \rho V_x \\ \rho E \\ \rho Y_{sp} \end{bmatrix}, G^* = \begin{bmatrix} \rho V_x \\ \rho V_x^2 + P \\ \rho V_x(\rho E + P) \\ \rho V_x Y_{sp} \end{bmatrix}, Q^* = \begin{bmatrix} 0 \\ 0 \\ 0 \\ \rho \dot{Y}_{sp,\text{chem}} \end{bmatrix}$$

Because each tube has a constant cross section area, A can be removed from the balancing equations. However, chemical composition is now changing in space and time. For this reason, additional balancing equations for each species mass fraction Y_{sp} are required and the Euler flow solver is coupled to a chemical kinetics solver via Strong splitting. Changes in composition as a result from chemical reactions $\dot{Y}_{sp,\text{chem}}$ are the only remaining source term, with the underlying reaction equations provided by the multi-step H_2–air mechanism published by Burke et al. [39].

At their outlets, all tubes are connected to a common plenum, represented by a zero-dimensional volume of fixed size $V_{\text{tp}} = 0.1\,\text{m}^3$. Boundary conditions at all tubes provide isentropic expansion of momentary tube pressure to momentary plenum pressure, while the specific axial kinetic energy is maintained. The resulting mass flow from the tubes into the plenum is taken as a mass and energy source term in the plenum's balancing equations. Since it is zero-dimensional, only mass, energy and species fractions are considered here, while velocity is assumed to be always negligible.

The outflow from the plenum is calculated based on interpolated experimental data from the same two-stage turbine as in the turbine models (see above) [23]. With an assumed constant turbine speed, the mass flow at the turbine inlet is a function of the plenum's temperature and the pressure ratio between plenum pressure and constant outlet pressure $P_{\text{out}} = 3.63\,\text{bar}$. The latter value was chosen to allow for average pressure ratios across the turbine that are close to its design point.

In addition to the plenum volume, the ratio between detonation tube cross section area A_{tube} and turbine inlet A_{turb} is another important parameter that defines the extent of pressure and temperature fluctuations in the

plenum. To ensure comparability between configurations with a varying number of tubes, this ratio is fixed to

$$\frac{A_{\text{tube}} \cdot n_{\text{tubes}}}{A_{\text{turb}}} = 1 \tag{5}$$

in all simulations, with n_{tubes} being the number of PDC tubes. This is roughly equivalent to enforcing the same average mass flow through the plenum and turbine model, regardless of n_{tubes}. Roughly only, because this neglects the additional mass coming from the fuel/combustion products, which is increased for a larger number of tubes and thus more ignitions during the same time interval. However, for the chosen operating frequency and tube length, this contribution is minuscule.

With fluctuating inflow of varying composition from the tubes and outflow to the turbine that depends on the current plenum state, pressure and temperature inside the plenum are subject to periodic change. The results of these simulations are discussed in Sec.3.2.1 and then used as boundary conditions for the calculations discussed in the remainder of Sec.3.2 and 3.3.

3. Results and discussion

In this section, the simulation tools are validated by comparing their results against experimental data. This is done only for steady-state operation, since only steady-state experimental results are available. Once this validation is carried out, the time-dependent boundary conditions produced by the PDC model will be elaborated. Subsequently, the turbine unsteady simulation results for the case with three PDC tubes will be presented. This section concludes with the presentation of turbine simulations using two alternative PDC configurations with five and seven tube with the aim to further evaluate the 1D-Euler method.

3.1. Model Validation

The turbine overall characteristic in terms of pressure ratio and efficiency is calculated using the meanline and 3D-CFD tools for the test case in question. Based on the available experimental data [23], the steady-state map is computed for three different total to static pressure ratios of 4, 5.5 and 7 spanning around the design reduced rotational speed point (see Table 1). The results of the steady-state calculations are depicted in Figure 7, noting that the isentropic efficiency curve is plotted only for total to static pressure ratio at the design point to avoid the complexity of the presentation. The results reveal that both the CFD and meanline method can accurately capture the steady-state performance of the two-stage turbine. A very small deviation between the results of the two computational methods and those of experiments is observable when moving away from the design point. This deviation takes its largest value at high speeds, which is nevertheless lower than 1% in pressure ratio and thus almost negligible. It is thus concluded that the meanline method is accurate enough to calculate the blade source terms for the 1D-Euler code.

In order to evaluate the validity of the 1D-Euler simulation, inter-stage thermodynamic properties of static pressure, static temperature, and total temperature throughout the turbine axis are calculated using the 1D-Euler, meanline, and 3D-CFD methods, depicted in Fig.8. It should be noted that the meridional sketch of the turbine in some figures in this paper is only for additional clarification of blade locations along the axial direction and does not represent the real shape of the blade. The CFD results are extracted at a plane between the blade rows and mass averaged values over the surface are reported.

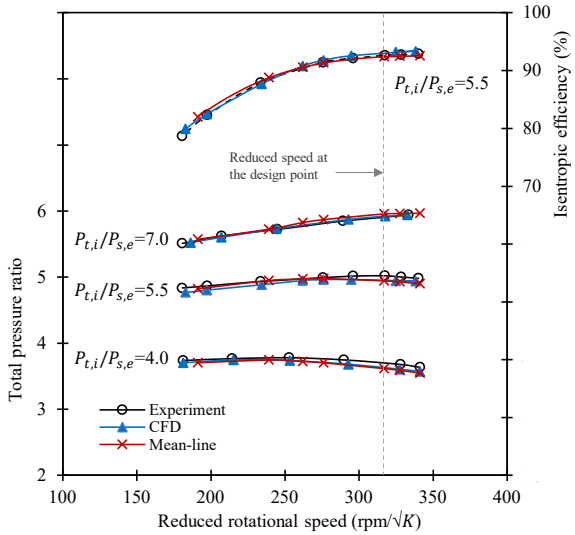

Figure 7: Turbine steady state performance characteristics, meanline, 3D-CFD and experiment [23]

The meanline results are computed exactly at the blade leading and trailing edges, and the 1D-Euler results are calculated throughout the turbine axial direction in each computational cell. The simulations were done at the turbine design point using the related fixed inlet total pressure and total temperature and outlet static pressure. The interstage static pressure distribution shows a very good match between the results, asserting that the 1D-Euler method can capture the static pressure through the machine very well. The total temperature distribution is also consistent between the three methods. Therefore, it can be concluded that the 1D-Euler code can effectively use the source terms from the meanline method to simulate the turbine operation. Also the interstage static temperature values are in agreement at stator inlets while there is a level of deviation at rotor inlets between the 1D-Euler and the two other methods. This mismatch can be explained by the nature of the 1D method. In CFD and meanline method, the axial velocity is used for mass calculation and the absolute velocity for kinetic energy. Since the only velocity component in the 1D method is axial velocity, both mass flow and kinetic energy calculations are done using the axial velocity. Therefore, wherever swirl is imparted by the vane and axial the velocity value deviates from that of the absolute velocity, there is a deviation in the kinetic energy calculation. In other words, the higher the tangential velocity, the lower the kinetic energy calculated in the 1D-Euler method compared to the CFD and meanline methods. Generally, in axial turbines, some level of swirl is added to the velocity by the stator rows, so that the tangential velocity increases. For more clarification, the velocity vectors around the second stator obtained by CFD are depicted within the Fig.8. It shows that the absolute velocity deviates from the axial direction at the stator exit, while it is mainly axial at the stator's inlet. For the stator rows, the only source term representing the blade is the force term, which includes axial velocity. As a result, the kinetic energy at the stator exit calculated from the 1D-Euler tool is lower than the actual value. Consequently, a higher static temperature value is computed in this tool compared to the results of the computed by CFD and meanline methods. Additionally, when the flow passes through the rotor blades, the extracted work reduces the swirl velocity and makes the flow axial at the rotor outlet. This occurs in reality, which is captured well in CFD and meanline, but in 1D-Euler simulation it is the axial velocity that is reduced. Therefore, the deviation in velocity at the stator outlet is compensated at the rotor outlet, which is obvious from a good agreement between the 1D-Euler, CFD, and meanline results of static temperature.

3.2. Unsteady turbine simulation

In this section, the unsteady simulation of the two-stage turbine connected to a plenum that is operated by a PDC configuration is elaborated. The PDC configuration includes three tubes, which produce a relatively high amplitude of fluctuations. The PDC model and the related

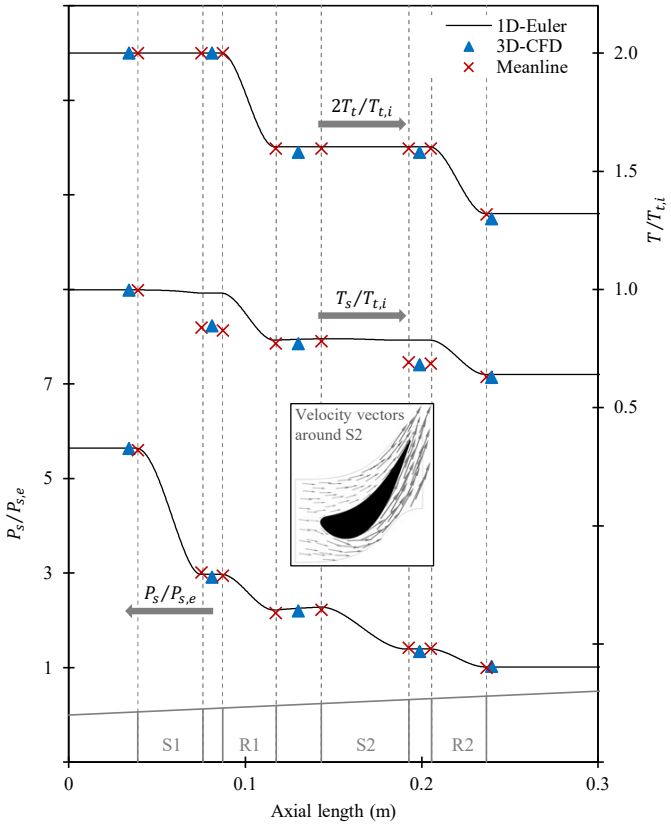

Figure 8: Streamwise distribution of thermodynamic parameters at the design point

boundary condition of the turbine will be explained hereafter. A back-to-back comparison of CFD and 1D-Euler unsteady simulation results will be done to evaluate the applicability of the latter method in unsteady simulation of the turbine.

3.2.1. Boundary condition for the time dependent turbine simulations

The resulting turbine plenum pressure for three variants of the multitube PDC configuration introduced in Sec.2.4.2 can be seen in Fig.9(a). After a short transient starting phase, a periodic pattern emerges for all three tube numbers. With each individual tube's operating frequency fixed at 20 Hz, the repetition frequency of this pattern is equal to $n_{\text{tubes}} \cdot 20\,\text{Hz}$. Table3 lists the average, maximum and minimum pressure observed for each of the configurations. It also calculates the relative pressure fluctuation amplitude defined in Eq.6.

$$\overline{A_P} = \frac{P_{max} - P_{min}}{\frac{2}{\tau}\int_{t_0}^{t_0+\tau} P_{tp}\,dt} \tag{6}$$

Table 3: Turbine plenum pressure fluctuations

n_{tubes}	P_{mean} (bar)	P_{max} (bar)	P_{min} (bar)	$\overline{A_P}$ (%)
3	21.67	27.00	17.68	21.5
5	21.33	23.25	19.13	9.7
7	21.20	22.45	19.61	6.7

An increase in the number of PDC tubes significantly reduces the fluctuation amplitude inside the turbine plenum due to the fact that each tube's relative contribution to the overall mass flow is reduced, ensured by the condition set in Eq.5. This also explains why the effect is far more pronounced for an increase from three to five tubes than it is from five tubes to seven. The mean pressure inside the plenum remains mostly constant for all three configurations, because it is primarily a result of the average mass flow, which also remains constant (except for the amount of fuel, as pointed out before).

For a closer analysis of the fluctuation pattern inside the plenum, Fig.9(b) shows pressure and temperature evolution during a single 60 Hz cycle of the configuration with three PDC tubes. The dashed lines connect this pattern to states inside the PDC tubes at the same moment, which were depicted in Fig.6. The last ignition inside one of the tubes took place at ①. It is only after the detonation wave has completed its propagation through the tube (②) and reaches the plenum inlet, that a steep increase in plenum pressure and temperature is visible. While the pressure increase is halted after a few ms due to increased outflow towards the turbine and the propagation of expansion waves upstream into the PDC tube, temperature remains high for about two thirds of the overall cycle, even though purge

air begins to flow into the inlet of the PDC tube already at ③. The reason for this seeming phase shift between pressure and temperature lies in the vast difference in their characteristic velocities: The local speed of sound inside the combustion products is very high due to their extreme temperature, allowing pressure waves to travel fast and quickly mitigate fluctuations and even causing temporary overexpansion that results in a slow increase of pressure during the latest third of the cycle. At the same time, also due to the inviscid nature of the numerical model, temperature perturbations only travel at the local flow velocity, which is much smaller. Thus, the decrease in plenum temperature coincides with the arrival of the contact surface between combustion products and purge air at the plenum inlet.

Both turbine plenum pressure and temperature obtained by this method for a configuration with three PDC tubes are used as inlet boundary conditions for the 1D and 3D simulations discussed in the following sections. The results for five and seven tubes are used in the comparison presented in Sec.3.3. Here it is noted that the physical rotational speed (12630 rpm) and the static pressure at the domain outlet (3.63 bar) are kept constant in the unsteady turbine simulations. Different lengths of outlet domain were modeled and the results of the unsteady simulations showed that the turbine completely damps the inlet pressure fluctuation. Therefore, in this paper, the constant outlet pressure boundary is reasonable in the unsteady simulations.

3.2.2. Pressure damping

The fluctuating flow coming from the PDC tubes causes the turbine blades to work under off-design conditions, since the inlet velocity and the incidence angle are continuously deviating from their design values. The

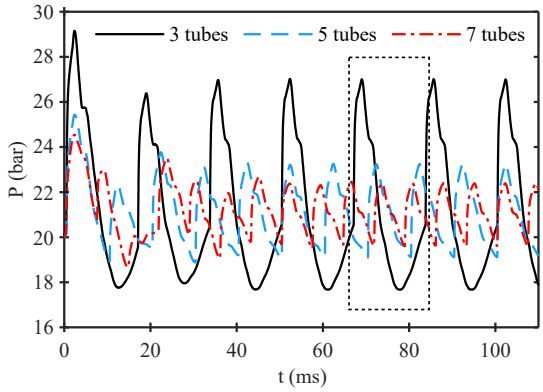

(a) Turbine plenum pressure for varying number of PDC tubes, marked area depicted enlarged in Fig.9(b) for three tubes

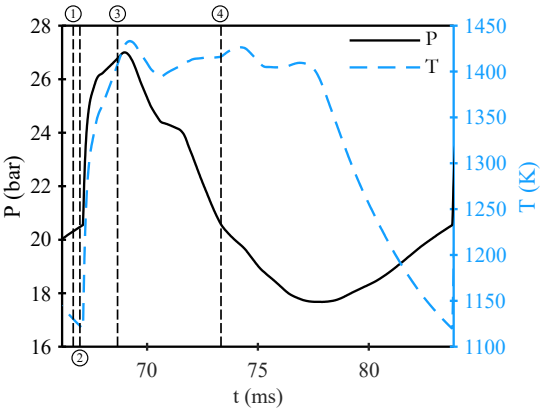

(b) Turbine plenum and temperature during a single fluctuation cycle for three PDC tubes, dashed lines mark tube states depicted in Fig.6

Figure 9: Time-resolved turbine plenum state

pressure fluctuation is expected to be damped throughout the turbine stages, with the damping level of each blade row being different. This causes the turbine rows to operate in different off-design ranges. The pressure distributions between the stages, obtained by the 1D-Euler and CFD methods, are shown in Fig.10 in the form of normalized pressure ($\overline{P_s} = P_s/mean(P_{s,i})$) for a cycle time period. The CFD results are mass-averaged values. The planes of measurement are located exactly between the blade rows, except for the first stator inlet and the last rotor outlet, which are located exactly adjacent to the blade row leading and trailing edge, respectively. According to the results, the trend of pressure distribution is almost

identically computed using both methods. Additionally, the pressure upstream of the stators is predicted similarly by both methods as well. Nevertheless, the 1D-Euler computed the pressure at stator outlets lower than CFD, which is traceable from a downshift in both Fig.10(c) and Fig.10(e). The difference is related to the flow direction at these two locations. The stators deflect the axial incoming flow to increase tangential momentum for the downstream rotors. Therefore, the absolute velocity magnitude is deviating from the axial velocity, while the latter is the only velocity component used in the 1D-Euler approach. Having a detailed look at the peak pressure location from upstream to downstream of the turbine, a small phase shift is observable. This is related to the axial distance and the local speed of sound because the prescribed pressure fluctuation propagates at the speed of sound. It is reminded that this in turn is related to the local temperature, which itself is advected by the flow velocity.

To evaluate the pressure fluctuation damping throughout the turbine, the relative static pressure amplitude defined in Eq.6 is calculated and depicted in Fig.11.

Starting from the domain inlet up to the first stator leading edge, both the 1D-Euler and CFD methods computed the static pressure amplitude identically, which is evident from Fig.10(a) and Fig.10(b) as well. Considering the boundary condition applied to the domain inlet in the form of total pressure in both methods, it implies that the kinetic energy is calculated the same at this point. After passing the first stator, a slightly higher relative pressure amplitude is calculated by CFD, with a difference of less than 0.5%. Moving further downstream shows a good match in relative pressure amplitude at the first rotor and the second stator outlet. A very small discrepancy between the values computed by CFD compared to those of 1D-Euler downstream of the second rotor blade row can be seen. This difference may be explained by the damping role of endwall viscous effects. The static pressure at the domain outlet is fixed in both methods as the outlet boundary condition. Since the 1D-Euler does not take into account the end wall viscous effects in between blade rows, the CFD calculation shows slightly more damping from the second rotor outlet to the domain outlet, where the static pressure has no fluctuation.

Regarding the damping of the pressure fluctuations, it is evident that the share of the first stator in damping is much higher than the other rows. The first stator damps 45.5% of the high-amplitude pressure fluctuation imposed at the domain inlet. This is consistent with the work of Bakhtiari et al. [34] that shows a 47% damping by the first row. It is noted that they prescribed a sinusoidal pressure fluctuation with an amplitude of 5% at the domain inlet, which is much lower than in the present study. The rest of the fluctuation amplitude is attenuated by the other rows.

3.2.3. Efficiency

Isentropic efficiency is defined as the actual work output from the turbine divided by the work output if the turbine with the same pressure ratio undergoes an isentropic process as in Eq.7. In steady-state operation, both terms can be simply calculated. In unsteady cases, where the turbine is subject to unsteady periodic inlet flow, the calculation of the isentropic efficiency is not straightforward through the well-known expression in Eq.8. In this case, the instantaneous inlet and outlet conditions cannot be used in efficiency calculation since the mass and energy fluxes are not conserved.

$$\eta_{isentropic} = \frac{\Delta H_{actual}}{\Delta H_{ideal}} \tag{7}$$

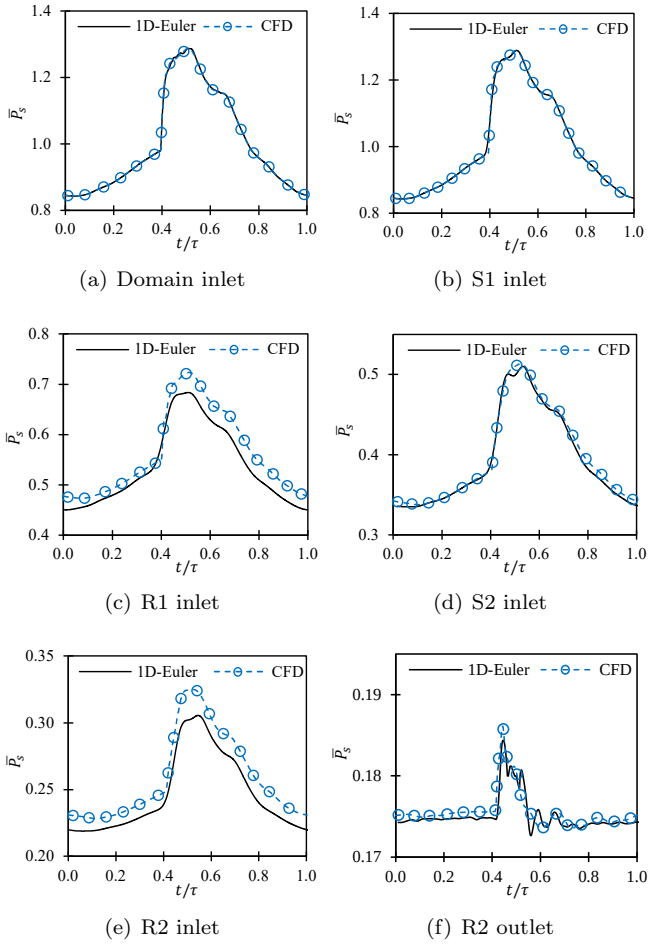

(a) Domain inlet (b) S1 inlet

(c) R1 inlet (d) S2 inlet

(e) R2 inlet (f) R2 outlet

Figure 10: Static pressure distribution over an inlet fluctuation time period at interstage locations

$$\eta_{isentropic} = \frac{1 - T_{t,e}/T_{t,i}}{\left[1 - \left(\frac{P_{t,e}}{P_{t,i}}\right)^{(\gamma-1)/\gamma}\right]} \tag{8}$$

The current work utilizes for efficiency calculations the definition proposed by Suresh et al. [40] for a turbine downstream a pulse detonation combustor. Taking into account that mass and energy fluxes are conserved within a time period of unsteadiness, the actual turbine work will be as Eq.9.

$$\Delta H_{actual} = c_p \int_0^{\tau} \left(\rho_i V_{x,i} A_i T_{t,i} - \rho_e V_{x,e} A_e T_{t,e}\right)\, dt \tag{9}$$

To calculate the ideal work output, the "theoretical

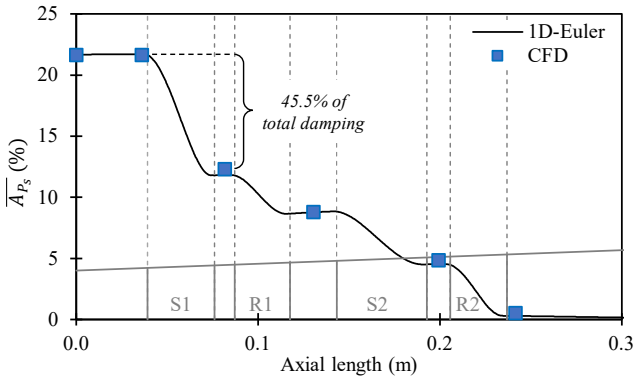

Figure 11: Static pressure damping throughout the turbine

isentropic" turbine is considered to work between the same inlet and outlet boundary conditions of the actual turbine. Hence, a flow particle entering the turbine at t_1 with all thermodynamic quantities related to t_1 exits at t_2 having the related time-dependent quantities. If it is assumed that the expansion process in the turbine is sufficiently fast, so that the difference between t_1 and t_2 is negligible, the ideal extracted work can be calculated by Eq.10. This assumption has been discussed in detail by Suresh et. al [40].

$$\Delta H_{ideal} = c_p \int_0^{\tau} \rho_i V_{x,i} A_i T_{t,i} \left[1 - \left(\frac{P_{t,e}}{P_{t,i}}\right)^{(\gamma-1)/\gamma}\right] dt \tag{10}$$

Using Eq.9 and 10, the isentropic efficiency in unsteady turbine operation can be calculated through Eq.7. Since in this approach, the time traces in both actual and ideal work calculations are fixed, it is more realistic than the time-averaged efficiency, which uses the averaged flow quantities at inlet and outlet in Eq.8. The isentropic efficiencies calculated based on the 1D-Euler and CFD simulation results are outlined in Table4. The steady-state efficiency reported here is out of the 3D-CFD turbine simulation while the boundary conditions are imposed equal to the mean value of the transient boundary conditions.

According to the CFD calculated value, a decrease of

Table 4: Isentropic efficiency of the turbine working with three PDC tubes

	3D-CFD	1D-Euler	Steady-state
Efficiency (%)	89.5	88.1	92.4

2.9% in efficiency is seen by moving from steady-state operation to the transient turbine operation. The efficiency deviation between the 1D-Euler and the 3D-CFD simulations is 1.4 percentage points. To inquire into this difference, time-dependent total pressure and total temperature at the outlet are plotted in Fig.12. Here, it is to be remembered that the CFD results are mass-averaged values. Fig.12(a) shows that the 1D-Euler solver predicted the total pressure at the domain outlet relatively similar to its CFD counterpart within the second half of the time period, while the overall trend is identical. The maximum relative difference, which lies within the first half of the time period, is 1.7%. The other cause for the efficiency difference between the two methods is related to the total temperature prediction. According to Fig.12(b), the 1D-Euler simulation results in a higher total temperature at the turbine outlet with an instantaneous maximum relative difference of 4.1%. This difference indicates that the work extracted from the turbine as computed by the 1D-Euler is lower than the actual value, which is related to the work source term for rotor blades. Since the source terms are looked up from the meanline-derived values based on static pressure around the blades, the discrepancy already reported in static pressure upstream of the rotor blades may cause the solver to read a lower work value from the source terms table. Again, both methodologies can capture a similar trend in total temperature very well.

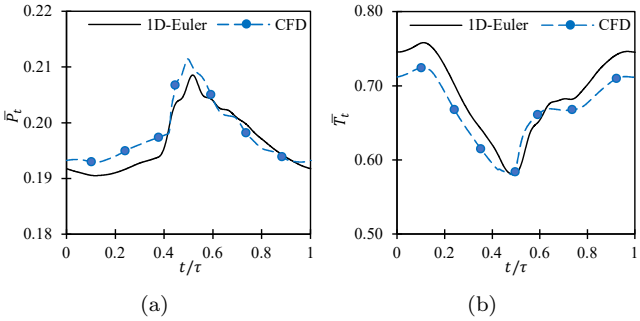

Figure 12: Normalized total pressure (a) and total temperature (b) at the turbine outlet over a time period

3.2.4. Performance characteristics

The turbine operating map is usually represented by a function of its pressure ratio and reduced mass flow This function is a single curve for each rotational speed and includes several possible steady-state operating points of the turbine. In the case of periodic unsteady inflow, the turbine operating condition is no longer a single curve on the characteristic map but illustrated by closed loops of points. The shape and size of the characteristic loops depend on the shape, amplitude, and frequency of the pulsed inflow [41]. The characteristic hysteresis loops computed by both 3D-CFD and 1D-Euler methods are shown in Fig.13(a), in which the steady-state characteristic line is plotted by a dashed line for reference. Since the inlet total temperature is time-dependent and the physical rotational speed is constant, the reduced speed ($rpm/\sqrt{K}$) is a function of time too. The steady characteristic curves for different reduced speeds lie on top of each other and create a single constant reduced mass flow line because the range of operation is within the choked flow condition. To explain the unsteady behavior of the turbine, the unsteady map can be traced back to the local gradient of inlet pulsed flow quantities. According to the inflow pulse shown in Fig.13(b), from point a to b, where inlet total pressure is building up but the total temperature is decreasing rather smoothly,

the reduced mass flow is kept constant, identically predicted by both methods. From b to c, a sharp increase in both total pressure and total temperature causes the instant pressure ratio and reduced mass flow to increase rapidly, up to the maximum reduced mass flow. From c to d, the pressure ratio keeps its increasing trend and reaches a maximum value at point d, which is before maximum inlet total pressure, where the steep slope ends. Afterward, from d to a, the pressure ratio decreases while maintaining an almost constant reduced mass flow. In this region, there are some small loops in the unsteady map mainly because of the inlet total temperature that has some small perturbations.

The unsteady hysteresis loops obtained by both methods have the same shape and the reduced mass flow range is identically predicted. The only difference is related to the instant pressure ratio and reduced mass flow within the filling zone between point b and d, where a very sharp increase in inlet total quantities is imposed by the boundary conditions. To put it another way, generally, the information from the inlet boundary in the form of pressure and temperature is transferred to the outlet with the speed of sound and flow speed, respectively. Hence, even small differences in temperature or velocity between both methods result in a phase shift in terms of the instantaneous total pressure at the domain outlet and subsequently the pressure ratio predicted by each method. This phase shift comes into view when the instantaneous pressure ratio is plotted over the reduced mass flow rate, which is calculated based on the information at the domain inlet. Since the mass flow is not conserved at every instant, the present little difference in instant pressure ratio in the unsteady map is plausible. Furthermore, the non-symmetrical shape of the hysteresis loop around the steady-state characteristic

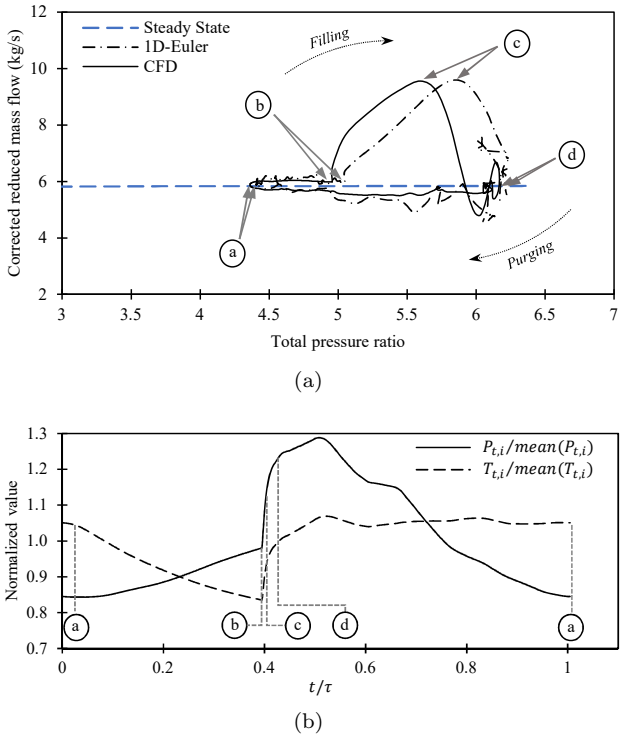

Figure 13: Turbine hysteresis loop over the steady state characteristic line (a) and the total quantities imposed at the turbine inlet boundary (b)

line is explained by the shape of inlet flow fluctuation, which is not a smooth and symmetrical pulse. In this regard, the hysteresis loop deviates considerably from the steady-state line within the region of high-gradient in inlet flow properties. In this region, the change in pressure over time is not slow enough to create a balanced state between the pressure ratio and mass flow rate. Obviously, the hysteresis gets closer when the gradient in inlet flow is moderate. It is expected in a smoother shape of inlet flow fluctuation, the hysteresis loop encapsulates the steady map curve rather symmetrically, as observed in ref.[17] for a mixed flow turbine.

3.3. Results for different PDC configurations

The applicability of the methodology for turbine simulation under pulse detonation combustion flow is further evaluated by changing the number of PDC-tubes in the combustor configuration. In this section, the sim-

ulation results for the PDC-turbine configurations with five and seven tubes will be presented. Compared to the three-tube configuration, the two new configurations provide unsteady turbine inlet flows with higher frequencies ($f_{5tubes} = 100Hz,\ f_{7tubes} = 140Hz$) and lower amplitudes ($\overline{A_{Ps,5tubes}} = 9.7\%,\ \overline{A_{Ps,7tubes}} = 6.7\%$). Therefore, it is expected that the turbine performance is less affected by the unsteadiness. For this reason, instead of repeating all the results previously presented for the three-tube configuration, this section only focuses on the efficiency and pressure damping characteristics.

Table5 outlines the time-resolved efficiency of the turbine for both configurations obtained by CFD and 1D-Euler methods. It is observed that by increasing the number of PDC tubes and consequently lowering fluctuation amplitude, the efficiency predicted by both methods increases. The change in CFD calculated efficiency from three to five-tube and five to seven-tube configurations are 0.8% and 0.2% respectively (the same trend is observed for 1D-Euler calculated efficiencies). Regarding the difference between the efficiency calculated by the two methods, the 1D-Euler predicted lower values ($\leq 1.1\%$) than the CFD counterpart as previously observed for three tubes. However, as the fluctuation amplitude decreases, the deviation between the 1D and 3D-CFD efficiency diminishes, so that in the case with seven tubes the 1D-Euler underpredicts the efficiency by just 0.8 percentage points. The turbine output power is also computed here as a performance parameter. The time-averaged turbine power values are 337.7 kW, 343.8 kW and 347.0 kW for 3, 5 and 7-tubes configurations, respectively. As is expected, increasing the number of PDC tubes raises turbine power. The 3D-CFD computed turbine power values are almost identical to those of 1D-Euler results, considering the fact

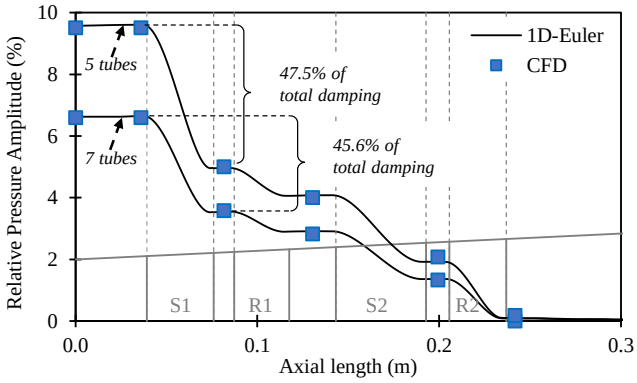

Figure 14: Static pressure damping for five and seven PDC tubes

that the 1D-Euler solver uses the prescribed force and energy source terms in the equations.

Table 5: Turbine isentropic efficiency for all combustor configurations

	3D-CFD	1D-Euler
Efficiency (%), 3-tubes config.	89.5	88.1
Efficiency (%), 5-tubes config.	90.3	89.2
Efficiency (%), 7-tubes config.	90.5	89.7

Pressure damping is evaluated for the two configurations by both methods, depicted in Fig.14. It is seen that the 1D-Euler solver delivers very close results to what is obtained through the CFD simulations and the trends are well captured as well. A quantitative look at the damping results indicates that 47.1% and 45.6% of the total inlet fluctuation are damped while the unsteady inlet flow passes through the first row in five and seven-tube configurations, respectively. Having captured almost the same result for the three-tube case in Fig.11 and the damping reported by Bakhtiari et al. [34] applying a different inlet boundary condition, at this point, it can be concluded that the amount of damping through the blade rows depends more on the geometry than the flow fluctuation features. More investigations are required to generalize this claim.

The deviation of mass flow rate by the 1D-Euler from the 3D-CFD computed values as a metric involved in hysteresis loops is calculated to quantify the model accuracy

in the instantaneous mass flow prediction. The instantaneous mass flow rate difference is normalized by the maximum values for each configuration ($\delta_m = \frac{\dot{m}_{1D} - \dot{m}_{CFD}}{\dot{m}_{max}}$). In Sec.3.2.4, it was shown that the mass flow range is accurately captured by the 1D-Euler method for the configuration with three PDC tubes, when it is compared with the CFD results. This is also observed in the results for the two current configurations, which are not repeated graphically here. Figure15 depicts the distribution of instantaneous deviation in mass flow rate in the form of a histogram. The horizontal axis indicates the percentile of mass flow deviation and the vertical axis represents the number of instantaneous mass flow rate points normalized by the total points in each configuration. According to the histogram of all of the configurations, more than 80% of the instantaneous mass flow rate points have a deviation within $\mp$5% (83% in 3tubes, 81.3% in 5tubes and 80.5% in 7tubes). This is consistent with Fig.13(a) indicating the main difference in the hysteresis loops of 1D-Euler and CFD is between the points b and d, which corresponds to a short time within a time period shown in Fig.13(b). This confirms that within the majority of the fluctuation time period, the 1D-Euler method predicts the instantaneous turbine performance well compared to the 3D-CFD results.

4. Conclusions

A fast and reliable tool for turbine unsteady simulation in conjunction with PDC arrays has been presented and evaluated. The method integrates a 1D-Euler, an in-house meanline analysis program and a PDC numerical model. The latter takes the steady-state turbine performance and delivers the unsteady boundary conditions for unsteady turbine simulations. The meanline method also provides

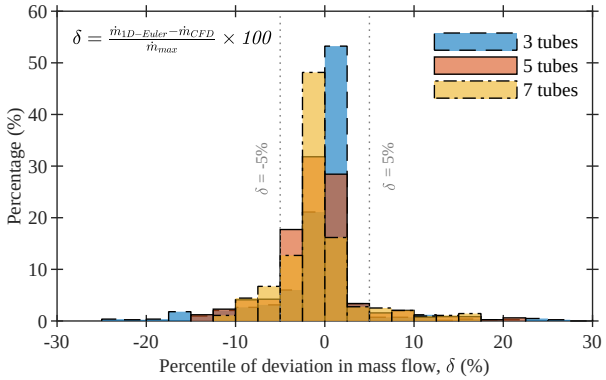

Figure 15: Histogram of mass flow rate deviation for turbine working with different PDC configurations

the source terms for the 1D-Euler solver. The developed approach was run using three different combustor configurations providing different boundary conditions for the turbine. A back-to-back comparison of the results with those of unsteady 3D-CFD was done to evaluate the accuracy of the approach. A summary of the main outcomes is as follows.

The PDC numerical scheme simulated three PDC-plenum configurations having three, five, and seven tubes. The simulation results provide the time-dependent pressure and temperature in the plenum. For all configurations, a periodic pattern with a frequency depending on the number of tubes and the tubes' individual operating frequency emerged inside the plenum. It was shown that increasing the number of PDC tubes while maintaining the overall area ratio between combustion chambers and turbine inlet significantly mitigates the amplitude of the fluctuations. Temperature and pressure evolution inside the plenum displays a phase shift that can be attributed to the difference in their characteristic velocity of information, one being the local speed of sound and the other one being the flow velocity.

The unsteady simulation results of both 1D-Euler and 3D-CFD showed that the two-stage turbine is capable of

damping the fluctuations throughout the stages. Additionally, it was indicated that the first row has a considerable damping role (around 45%), irrespective of the imposed fluctuation amplitude at the inlet boundary.

In terms of isentropic efficiency, unsteady simulations by both 3D-CFD and 1D-Euler showed an efficiency drop of up to 3% compared to the corresponding steady-state operation. In general, the isentropic efficiency calculated by the 1D-Euler is lower than that predicted from the 3D-CFD, while this discrepancy becomes less with lower inlet fluctuation amplitudes.

The performance hysteresis loop of the turbine encapsulates the steady-state characteristic line, though it is not symmetrically distributed. The reason was explained by the sharp gradient in the inlet flow conditions within the filling zone. Both methods have identically captured the overall shape of the hysteresis. In this context, the instantaneous mass flow rate is well predicted by the 1D-Euler method compared to the 3D-CFD. The results indicate that the majority of the instantaneous reduced mass flow rate in a pulse cycle lies within $\mp 5\%$ deviation from the CFD-computed values.

All in all, the developed methodology based on the 1D-Euler showed its ability for simulating the multistage turbine working with pulsed detonation combustion exhaust flow. The deviation in the results compared to those of the unsteady 3D-CFDs is mainly because of the inherent nature of one-dimensional modeling, which does not fully consider circumferential and radial flow features. Nevertheless, the methodology is fast and accurate enough to provide a robust tool for performance evaluations of turbines specifically in early design and development stages, where still a multitude of different configurations is under consideration.

Finally, two early decisions made to ease the tool development and keep it as generalized as possible must be mentioned here. The first is that the current work neglected any entropy generation caused by shock waves in the plenum and at the turbine inlet. This can be easily corrected with additional entropy generation terms, in the existing 1D-Euler and plenum models. These terms should be however calibrated for the specific geometrical design of each plenum. The second decision was to neglect any cooling air injection both in the plenum and the turbine models. Again, this shortcoming can be easily corrected with mass source terms in both models. Although these decisions might have some limited impact on the quantitative results of the presented models, they have no effect on the basic qualitative results and the demonstrated fidelity of the suggested 1D-Euler modelling approach of the turbine.

Acknowledgement

The authors would like to acknowledge the financial support from Deutsche Forschungsgemeinschaft (DFG) as part of the Collaborative Research Center SFB 1029 in Project D01 as well as part of the research grant 317741329 and Elsa Neumann Foundation (NaFöG). Additionally, Norddeutsche Verbund für Hoch-und Hoechstleistungsrechnen (HLRN) is gratefully acknowledged for providing the high performance computing resources.

Abbreviations and Nomenclature

References

[1] International Civil Aviation Organization, Annual report of the council, Tech. rep., International Civil Aviation Organization (2019).

URL https://www.icao.int/annual-report-2018/Pages/

CJ	Chapman–Jouguet
E^3	Energy Efficient Engine
GCI	Grid Convergence Index
PDC	Pulsed Detonation Combustion
PGC	Pressure Gain Combustion
ZND	Zel'dovich, von Neumann, Döring
A	Cross sectional area
$\overline{A_P}$	Relative pressure amplitude
E	Internal energy
e	Error
f	Frequency
H	Total enthalpy
h	Specific enthalpy
L	Length of the PDC tubes
N	Number of nodes
$\dot{m}$	Mass flow rate
P	Pressure
$\overline{P}$	Normalized pressure
rpm	Round per minute
T	Temperature
$\overline{T_t}$	Normalized total temperature
V_x	Axial velocity
W	Work
Y	Mass fraction
y^+	Dimensionless wall distance
γ	Heat capacity ratio
δ_m	Mass flow deviation
ρ	Density
τ	Time period
$_b$	Bleed
$_{cp}$	Compressor plenum
$_e$	Turbine exit plane
$_i$	Turbine inlet plane
$_k$	PDC tube index
$_{rel.}$	Relative value
$_{sp}$	Species index
$_s$	Static quantity
$_t$	Total quantity
$_{tp}$	Turbine plenum

the-world-of-air-transport-in-2018.aspx#:~:text=The4.3billionairlinepassengers,some90millionin2040.

[2] E. Bach, P. Stathopoulos, C. O. Paschereit, M. D. Bohon, Performance analysis of a rotating detonation combustor based on stagnation pressure measurements, Combustion and Flame 217 (2020) 21–36. doi:https://doi.org/10.1016/j.combustflame.2020.03.017.

[3] T. A. Kaemming, D. E. Paxson, Determining the Pressure Gain of Pressure Gain Combustion, in: 2018 Joint Propulsion Conference, American Institute of Aeronautics and Astronautics, Reston, Virginia, 2018, pp. 1–15. doi:10.2514/6.2018-4567.

[4] J. Tellefsen, Build Up and Operation of an Axial Turbine Driven by a Rotary Detonation Engine, Ph.D. thesis, Air Force Institute of Technology (2012).

[5] P. Wolański, Application of the Continuous Rotating Detonation to Gas Turbine, Applied Mechanics and Materials 782 (2015) 3–12. doi:10.4028/www.scientific.net/AMM.782.3.

[6] J. A. T. Gray, J. Vinkeloe, J. Moeck, C. O. Paschereit, P. Stathopoulos, P. Berndt, R. Klein, Thermodynamic Evaluation of Pulse Detonation Combustion for Gas Turbine Power Cycles, in: Volume 4B: Combustion, Fuels and Emissions, ASME, 2016, p. V04BT04A044. doi:10.1115/GT2016-57813.

[7] C. Xisto, O. Petit, T. Grönstedt, A. Rolt, A. Lundbladh, G. Paniagua, The efficiency of a pulsed detonation combustor–axial turbine integration, Aerospace Science and Technology 82-83 (August) (2018) 80–91. doi:10.1016/j.ast.2018.08.038.

[8] T. Sakurai, S. Nakamura, Performance and Operating Characteristics of Micro Gas Turbine Driven by Pulse, Pressure Gain Combustor, in: Volume 5: Controls, Diagnostics, and Instrumentation; Cycle Innovations; Cycle Innovations: Energy Storage, American Society of Mechanical Engineers, 2020. doi:10.1115/GT2020-15000.

[9] P. Stathopoulos, An alternative architecture of the Humphrey cycle and the effect of fuel type on its efficiency, Energy Science & Engineering 8 (10) (2020) 3702–3716. doi:10.1002/ese3.776.

[10] A. Glaser, N. Caldwell, E. Gutmark, Performance of an Axial Flow Turbine Driven by Multiple Pulse Detonation Combustors, in: 45th AIAA Aerospace Sciences Meeting and Exhibit, no. January, American Institute of Aeronautics and Astronautics, Reston, Virigina, 2007, pp. 1–10. doi:10.2514/6.2007-1244.

[11] V. Anand, A. St. George, E. Knight, E. Gutmark, Investigation of pulse detonation combustors — Axial turbine system, Aerospace Science and Technology 93 (2019) 105350. doi:10.1016/j.ast.2019.105350.

[12] H. Qiu, C. Xiong, L. Zheng, Experimental investigation of an air-breathing pulse detonation turbine prototype engine, Applied Thermal Engineering 104 (2016) 596–602. doi:10.1016/j.applthermaleng.2016.05.077.

[13] A. Naples, J. Hoke, R. Battelle, F. Schauer, T63 Turbine Response to Rotating Detonation Combustor Exhaust Flow, Journal of Engineering for Gas Turbines and Power 141 (2) (2019) 1–8. doi:10.1115/1.4041135.

[14] D. Van Zante, E. Envia, M. G. Turner, The Attenuation of a Detonation Wave By an Aircraft Engine Axial Turbine, in: 18th ISABE Conference, no. ISABE-2007-1260, 2007, pp. 1–12.

[15] Z. Liu, J. Braun, G. Paniagua, Characterization of a Supersonic Turbine Downstream of a Rotating Detonation Combustor, Journal of Engineering for Gas Turbines and Power 141 (3) (2019) 1536–1539. doi:10.1115/1.4040815.

[16] M. Asli, P. Stathopoulos, C. O. Paschereit, Aerodynamic Investigation of Guide Vane Configurations Downstream a Rotating Detonation Combustor, Journal of Engineering for Gas Turbines and Power 143 (6). doi:10.1115/1.4049188.

[17] M. Yang, K. Deng, R. Martines-Botas, W. Zhuge, An investigation on unsteadiness of a mixed-flow turbine under pulsating conditions, Energy Conversion and Management 110 (2016) 51–58. doi:10.1016/j.enconman.2015.12.007.

[18] S. R. Taddei, Time-marching solution of transonic flows at axial turbomachinery meanline, Proceedings of the Institution of Mechanical Engineers, Part G: Journal of Aerospace Engineering (2020) 095441002097735doi:10.1177/0954410020977350.

[19] T. K. J. B. Michel Feidt, Paweł Ziółkowski, The efficiency of turbomachinery in the zero- and three-dimensional approaches, Entropy: Thermodynamics – Energy – Environment – Economy 1 (Issue 3). doi:10.21494/ISTE.OP.2021.0620.

[20] M. S. Chiong, S. Rajoo, A. Romagnoli, A. W. Costall, R. F. Martinez-Botas, Integration of meanline and one-dimensional methods for prediction of pulsating performance of a turbocharger turbine, Energy Conversion and Management 81 (2014) 270–281.

[21] L. Dittmar, P. Stathopoulos, Numerical Analysis of the Stability and Operation of an Axial Compressor Connected to an Array of Pulsed Detonation Combustors, in: Proceedings of the ASME Turbo Expo 2020, ASME, 2020. doi:10.1115/GT2020-15381.

[22] N. Neumann, M. Asli, N. Garan, D. Peitsch, P. Stathopoulos, A fast approach for unsteady compressor performance simulation under boundary condition caused by pressure gain combustion, Applied Thermal Engineering 196 (2021) 117223. doi:https://doi.org/10.1016/j.applthermaleng.2021.117223.

[23] L. P. Timko, Energy Efficient Engine High Pressure Turbine Component Test Performance Report, Tech. Rep. NASA Contract Report 168289, General Electric Co. Cincinnati, OH, United States (1984).

[24] I. B. Celik, U. Ghia, P. J. Roache, C. J. Freitas, H. Coleman, P. E. Raad, Procedure for Estimation and Reporting of Uncertainty Due to Discretization in CFD Applications, Journal of Fluids Engineering 130 (7) (2008) 078001. doi:10.1115/1.2960953.

[25] J. Sousa, G. Paniagua, J. Saavedra, Aerodynamic response of internal passages to pulsating inlet supersonic conditions, Computers and Fluids 149 (2017) 31–40. doi:10.1016/j.compfluid.2017.03.005.

[26] J. P. Clark, E. A. Grover, Assessing Convergence in Predictions of Periodic-Unsteady Flowfields, Journal of Turbomachinery 129 (4) (2007) 740–749. doi:10.1115/1.2720504.

[27] A. Sadagopan, C. Camci, Viscous flow and performance issues in a 6:1 supersonic mixed-flow compressor with a tandem diffuser, Aerospace Science and Technology 88 (2019) 9–21. doi:10.1016/j.ast.2019.02.027.

[28] M. G. Adams, P. Adami, M. Collins, P. F. Beard, K. Chana, T. Povey, Impact of rotor-casing effusion cooling on turbine performance and operating point: an experimental, computational, and theoretical study, Journal of Turbomachinery 143 (March) (2021) 1–24. doi:10.1115/1.4050019.

[29] N. Neumann, D. Peitsch, Introduction and validation of a mean line solver for present and future turbomachines, in: Proceedings of ISABE Canberra 2019, Canberra, Australia, 22-26 September, ISABE-2019-24441, 2019.

[30] R. H. Aungier, Turbine Aerodynamics: Axial-Flow and Radial-Flow Turbine Design and Analysis, ASME Press, 2006.

[31] J. D. Denton, Throughflow Calculations for Transonic Axial Flow Turbines, Journal of Engineering for Power 100 (2) (1978) 212–218. doi:10.1115/1.3446336.

[32] P. M. Came, Streamline Curvature Throughflow Analysis of Axial-Flow Turbines, in: 1st European conference, Vol 1; Computational methods, VDI Verlag, 1995, pp. 291–308.

[33] P. Berndt, R. Klein, Modeling the kinetics of the Shockless Explosion Combustion, Combustion and Flame 175 (2017) 16–26. doi:10.1016/j.combustflame.2016.06.029.

[34] F. Bakhtiari, H.-P. Schiffer, Numerical approach to the modelling of transient interaction of prospective combustor concepts and conventional high pressure turbines, Propulsion and Power Research 8 (1) (2019) 1–12. doi:10.1016/j.jppr.2019.01.008.

[35] Y. Zel'dovich, To the question of energy use of detonation combustion, J. Propuls. Power 22 (3) (2006) 588–592. doi:10.2514/1.22705.

[36] J. Von Neumann, Theory of detonation waves, in: A. J. Taub (Ed.), John von Neumann, collected works, Vol. 6, Macmillan, New York, 1942.

[37] W. Döring, Über den Detonationsvorgang in Gasen, Ann. Phys. 435 (6-7) (1943) 421–436. doi:10.1002/andp.19434350605.

[38] P. Holloway, C. Koch, G. Knight, S. Shaffer, Energy efficient engine - high pressure compressor detail design report, NASA-CR-165558, 1982.

[39] M. P. Burke, M. Chaos, Y. Ju, F. L. Dryer, S. J. Klippenstein, Comprehensive H2/O2 kinetic model for high-pressure combustion, International Journal of Chemical Kinetics 44 (7) (2012) 444–474. doi:10.1002/kin.20603.

[40] A. Suresh, D. C. Hofer, V. E. Tangirala, Turbine Efficiency for Unsteady, Periodic Flows, Journal of Turbomachinery 134 (3) (2012) 034501. doi:10.1115/1.4003246.

[41] A. St. George, E. Gutmark, Trends in Pulsating Turbine Performance: Pulse-Detonation Driven Axial Flow Turbine, in: 50th AIAA Aerospace Sciences Meeting including the New Horizons Forum and Aerospace Exposition, no. January, American Institute of Aeronautics and Astronautics, Reston, Virigina, 2012, pp. 1–16. doi:10.2514/6.2012-769.